

A Coupled Thermo-Mechanical-Metallurgical Model Capturing Essential Transformations in the Welding of High Strength Low-Alloy Steels

Carlos Roberto Xavier¹ , Horácio Guimarães Delgado Junior², Célio de Jesus Marcelo³, Fabiane Roberta Freitas da Silva³ , Gabrielle Cristine Lemos Duarte Freitas³, José Adilson de Castro³ 

¹ Centro Universitário de Volta Redonda – UniFOA, Volta Redonda, RJ, Brasil.

² Universidade do Estado do Rio de Janeiro – UERJ, Resende, RJ, Brasil.

³ Universidade Federal Fluminense – UFF, Volta Redonda, RJ, Brasil.

How to cite: Xavier CR, Delgado Junior HG, Marcelo CJ, Silva FRF, Freitas GCLD, Castro JA. A coupled thermo-mechanical-metallurgical model capturing essential transformations in the welding of high strength low-alloy steels. *Soldagem & Inspeção*. 2021;26:e2617. <https://doi.org/10.1590/0104-9224/SI26.17>

Abstract: A well-known challenge is to predict the transformations occurring during the metal alloys welding aiming to control the weldment properties. Thus, this study presents a Thermo-Mechanical-Metallurgical model to numerically predict the thermal history, the solid-state phase transformations, the solidification microstructure and the hardness distribution during and after the welding of high strength low-alloy steels. The model was numerically implemented in an in-house computational code based on the Finite Volume Method, which allowed to dynamically track and calculate the volume fractions of ferrite, pearlite, bainite and martensite at the heat-affected zone, besides the formation and determination of dendrite arm spacing at the fusion zone, whereas the hardness distribution at the heat-affected zone was calculated by applying the phase mixture rule. For this, single-pass autogenous Gas Tungsten Arc Welding welds were numerically simulated and experimentally carried out on high strength low-alloy AISI 4130 steel samples, including their preheating to evaluate the effectiveness of the proposed model to simulate the workpieces welding in different initial thermal conditions and a close agreement between the calculated and experimental results were obtained.

Key-words: High strength low alloy steels; Welding; Thermo-Mechanical-Metallurgical model; Numerical simulation; Thermal history; Phase transformations; Hardness.

Um Modelo Termo-Mecânico-Metalúrgico Acoplado Capturando Importantes Transformações na Soldagem de Aços de Alta Resistência e Baixa Liga

Resumo: Um desafio bem conhecido é prever as transformações que ocorrem durante a soldagem das ligas metálicas com o objetivo de controlar as propriedades da solda. Desta forma, este estudo apresenta um modelo Termo-Mecânico-Metalúrgico para prever numericamente a história térmica, as transformações de fase no estado sólido, a microestrutura de solidificação e a distribuição de dureza durante e após a soldagem de aços de alta resistência e baixa liga. O modelo foi implementado numericamente em um código computacional próprio baseado no Método dos Volumes Finitos, o que permitiu rastrear e calcular dinamicamente as frações volumétricas de ferrita, perlita, bainita e martensita na zona afetada pelo calor, além da formação e determinação do espaçamento do braço dendrítico na zona de fusão, enquanto que a distribuição da dureza na zona afetada pelo calor foi calculada aplicando-se a regra da mistura de fases. Para tanto, soldas autógenas usando o processo Gas Tungsten Arc Welding de passe único foram simuladas numericamente e experimentalmente realizadas em amostras do aço de alta resistência e baixa liga AISI 4130, incluindo seu pré-aquecimento com o objetivo de avaliar a eficácia do modelo proposto para simular a soldagem de peças em diferentes condições térmicas iniciais, tendo sido obtida uma estreita concordância entre os resultados calculados e experimentais.

Palavras-chave: Aços alta resistência e baixa liga; Soldagem; Modelo Termo-Mecânico-Metalúrgico; Simulação numérica; História térmica; Transformações de fase; Dureza.

Received: 17 Feb., 2021. Accepted: 02 Aug. 2021.

E-mails: carlos.xavier@foa.org.br (CRX), enghoracio@gmail.com (HGDJ), cjmarcelo64@gmail.com (CJM), fabianesilva@id.uff.br (FRFS), gabriellecristine@id.uff.br (GCLDF), joseadilsoncastro@id.uff.br (JAC)



This is an Open Access article distributed under the terms of the [Creative Commons Attribution Non-Commercial License](https://creativecommons.org/licenses/by-nc/4.0/) which permits unrestricted non-commercial use, distribution, and reproduction in any medium provided the original work is properly cited.

1. Introduction

According to Zinigrad and Borodianskiy [1], one of the main tasks of modern metallurgy is the joining process, which can be conducted by welding, brazing, or soldering techniques with recent scientific works in this field focusing on understanding the physical processes, as well in the structural evolution and its correlation with the final properties of the metal or alloy, which makes necessary the knowledge of the interdisciplinary basics in chemistry, physics, mathematics and engineering in order to solve complex tasks. Thus, the involved multidisciplinary implies that the possibility of presenting a reliable software is a defiant goal for considering the complexity to couple and to dynamically solve several models representing the physical, chemical, mechanical and metallurgical phenomena interacting during the welding. According to Grong and Shercliff [2], there are several situations where the microstructural prediction is very valuable to control the final properties (e.g., the toughness of steel welds); to the knowledge of microstructural limits for process optimization (e.g., maximum welding speed) and when microstructure captures the coupling through a multi-stage process, giving opportunities for new alloys and process development (e.g., effect of prior forming and heat treatment on weldability). From this perspective, modeling and numerical simulation have been shown very helpful tools to predict the microstructural and mechanical behavior of the weldment, besides saving costs and time by reducing the need for sometimes lengthy and expensive experiments and tests, as well contributing for product quality increasing. According to Zacharia et al. [3], due to the many variables involved, it is expensive and time-consuming, if not impractical, to create an adequately large experimental database to understand and control the welding process. Therefore, the authors have mentioned that recourse is to simulate the welding process through a set of mathematical equations representing the essential physical processes of welding, besides concluding that the obtained results from the phenomenological models will be crucially dependent on the quality of the physical relations contained in the models and the trustworthiness of the input data. Thus, in order to get cost-effective in the development of the friction stir welding (FSW) process for steels, Ahmad et al. [4] have used numerical modeling for three-dimensional thermo-mechanical simulation with previously generated experimental temperature-dependent properties besides the innovative use of coupling Eulerian-Lagrangian applied to model the FSW process on steel. Jedrasiak et al. [5] have presented a finite element thermal model for linear friction welding applied to an instrumented weld in Ti6Al4V. The focus was the characteristics of the power at the weld interface estimated from the measured transverse velocity and the cyclic machine load since the mechanical properties of weld joints are directly dependent on the solidification structures in the fusion zone. Yu et al. [6] have investigated the solidification microstructure evolution during welding by using the phase-field modeling technique to understand the solidification dynamics and get useful guidance to optimize the welding process. In simulations carried out by Zhang et al. [7], the microstructural and thermo-mechanical models were coupled to analyze the processing thermal history and attain more accurate simulated mechanical properties of the FSSW (friction stir spot welded) joints. To study the effects of processing parameters on the formation of intermetallic compounds at the aluminum/steel interface, microstructural characteristics, and mechanical property of dissimilar weldments, Eyvazian et al. [8] used the VOF (volume of fluid) modeling method to simulate the underwater friction-stir welding (FSW) process for dissimilar joining between aluminum and steel.

It is well recognized that High Strength Low Alloy (HSLA) steels are a group with important applications in several engineering designs, requiring permanent research in order to exploit and optimize its already attractive properties and ensuring that it will be preserved when HSLA steels are submitted to a determined fabrication or repair procedure. Following this matter, Costa et al. [9] have evaluated the influence of input variables as current, tension, and travel speed on output variables as tensile strength and hardness at the HAZ in welds of HSLA API 5L X70 steel performed by the SAW (submerged arc welding) process aiming to obtain satisfactory empirical mathematical models for the response variables, based in the response surface methodology (RSM) and with the purpose of welding parameters optimization. On the other hand, the thermal history from the welding procedure can promote harmful microstructural changes in HSLA steels, affecting their major technological properties, such as toughness and corrosion resistance, and generating a high level of residual stresses, which could interact with an unfavorable microstructure. In this context, the AISI 4130 steel is a HSLA group containing 0.30% carbon nominal content besides Cr and Mo as hardening alloys. The AISI 4130 steel can easily form a martensitic structure after quenching or fast cooling, as normally occurs in fusion welding. According to Neto et al. [10], metallic materials have received special attention in the aerospace and defense areas, leading Brazil to take up the technological challenges concerning the production and processing of ultra-high-strength steels, among them the AISI 4130, due to its application in landing gears, small aircraft's engine cradles, besides general industries. Thus, the authors have used the LBW (Laser Beam Welding) process as an alternative to the traditional TIG (Tungsten Inert Gas) welding process in order to compare the effects of both processes on the microstructure and mechanical behavior of welds in AISI 4130 steel. According to Tseng and Shiu [11], the AISI 4130 is a HSLA widely used in structural components that require a high strength-to-weight ratio, such as aircraft engine mounts, oil and gas valves, or pumps. Thus, the authors have investigated the influence of thermal stability of powdered oxides on the joint penetration of TIG welding of HSLA AISI 4130 steel and comparing the results of microstructure and microhardness of the weldments. In addition to its ductility, Emamian et al. [12] have quoted the higher specific strength ratio of HSLA AISI 4130 steel. These characteristics enable the engineers to reduce the designs weight by using thinner thicknesses, increasing its applications in the aerospace, machinery, and motorsports industries. Thus, the authors pursued the optimal mechanical properties of HSLA AISI 4130 steel welded by the GTAW process using different filler wire compositions and pre-weldment and post-weldment heat treatments. In their study on fatigue in welded joints from the critical airplane structures, Nascimento et al. [13] have quoted the high mechanical strength

values and reasonable ductility of the hot-rolled AISI 4130 steel plates. Still, they have also pointed out the decrease of the mechanical properties in welded joints of AISI 4130 steel when submitted to the GTAW process, therefore, leading the authors to investigate the effects of GTAW repairs on the axial fatigue of welded joints of this material in airframe critical to the flight-safety.

In addition, the quality of the welding zones is strongly affected by the solidification process and microstructure evolution. Thus, Saadati et al. [14] have evaluated the role of solidification patterns on the hot cracking in welds of HSLA steel. The authors concluded on the importance of the PDAS (primary dendrite arm spacing) and the SDAs (secondary dendrite arms) in providing more interlocking around the weld centerline, increasing the centerline resistance to the experienced stresses occurring during solidification. In order to attain a better understanding of the importance of weld metal solidification, Di et al. [15] measured the primary and secondary dendrite arm spacing after welding of MMMS (modified medium manganese steel) by conventional and pulsed GMAW (gas metal arc welding) techniques. According to the authors, pulsed current restrained the dendrite growth in the welds, resulting in finer dendrites grains and improving the ductility of the weld joint. Yang et al. [16] evaluated the effects of dendrite arm spacing on the corrosion resistance and mechanical properties in laser-welded selective laser melted 304 stainless steel joints. According to the authors, compared to the SLMed based metal, the laser-welded joints exhibited coarser dendrite structure, lower microhardness, and tensile properties, but superior corrosion resistance.

In this study, an in-house computational code based on the Finite Volume Method (FVM) was applied to simulate essential transformations occurring during fusion welding of a HSLA AISI 4130 steel by coupling the numerical models to predict the thermal history, the diffusional and non-diffusional decomposition of the austenite in low alloy hypoeutectoid steels during cooling, the model for prediction of solidified structures at the fusion zone (FZ) and the model for hardness evolution at the heat-affected zone (HAZ).

2. Experimental Procedure

The material investigated in this work was HSLA AISI 4130 steel with chemical composition presented in Table 1.

Table 1. Chemical composition of HSLA AISI 4130 steel (wt. %).

C	Si	Mn	Cr	Mo	Ni
0.32	0.23	0.54	0.83	0.19	0.23

Single-pass autogenous GTAW weld was carried out on HSLA AISI 4130 steel plates with 50 x 160 x 10 mm using an inverter machine for TIG welding model MigPulse 4000 from Eutetic Castolin adapted for mechanized welding in order to produce a weld bead length of 140 mm. The welding procedure used a 2.4 mm diameter 2%-thoriated tungsten electrode in DCEN (Direct Current–Electrode Negative) polarity and argon as shielding gas to a flux rate of 15 l/min. The experiments were carried out with and without base material preheating, i.e., of the HSLA AISI 4130 steel plates. A torch was used to preheat the plate, and thermocouples attached to it and connected to a data acquisition unit have served to monitor its temperature. When the temperature of the plate reached the defined preheat value, that is, 250°C, the welding procedure was carried out. The welding parameters current, voltage and speed, are presented in Table 2.

Table 2. Welding parameters.

Arc voltage (volt)	Welding current (A)	Welding speed (mm s ⁻¹)	Thermal efficiency (η)	Heat input (kJ mm ⁻¹)
10	124	2.0	0.8	0.5*
10	124	2.0	0.8	0.5
14	350	2.0	0.8	2.0

*Preheating: 250°C

2.1. Microstructural characterization

After grinding and polishing, the samples were characterized by using the metallographic techniques based on light optical microscopy (LOM) and scanning electronic microscopy (SEM) to support ImageJ software for image analysis. Samples were sectioned perpendicular to the weld bead in a position equivalent to the length-half of the welded plates. The reagent used to analyze the microstructure was the LePera etchant, which consists of a solution composed of 4 g of picric acid diluted in 100 ml of ethylic alcohol and the stock solution, composed of 1 g of sodium metabisulfite (Na₂S₂O₅), which are diluted with each other in the 1:1 proportion, whereas to evaluate the dendrites it was used a solution composed by 3 g of picric acid, 0.5 ml of hydrochloric acid, 240 ml of distilled water and 10 drops of detergent.

3. Modeling

The present study deals with model implementation, which considers the coupled phenomena of the solid-state phase transformations, melting and solidification, temperature evolution, and hardness prediction in the HSLA steel welding. Autogenous welding, i.e., a fusion welding process without the addition of filler material, was chosen to avoid the influence of the material additions into the microstructural transformations. The computer code used in this study has been continuously updated and applied for different welding conditions. The general features of the model and computational implementations have been validated for different steels, geometries, and boundary conditions [17-20].

3.1. The energy conservation equation

In this study, fundamental thermal, mechanical and metallurgical phenomena occurring during the HSLA AISI 4130 steel welding were evaluated by means of numerical simulation. For this purpose, it is necessary to predict the temperature field dynamically coupled with the welding evolution and the material thermophysical properties, together with the kinetic models for solid-state phase transformations, melting, and solidification. The phenomena of heat transfer by radiation, convection, and conduction are taken into account coupled with mass transfer, melting, and solidification, while the thermophysical properties were assumed as dependent on the material composition and temperature. The energy equation for a general coordinate system is represented in compact form by Equation 1. In Equation 1 [17-20], ρ is the density ($kg.m^{-3}$); C_p is the specific heat ($kJ.kg^{-1}.K^{-1}$); k is thermal conductivity ($W.m^{-1}.K^{-1}$); u is the velocity field, which accounts for buoyancy-driven flow in the liquid pool or moving mesh to match the geometry changes due to the metal deposition or surface deformation in the welding pool; T is the temperature field and S is the source term, which accounts for all source or sinks due to arc to metal interaction, phase transformations, melting and solidification.

$$\frac{\partial}{\partial t}(\rho C_p T) + \text{div}[\rho C_p (\vec{u}) T] = \text{div}[k(\text{grad}(T))] + S \quad (1)$$

The initial condition is assumed with the workpiece set up to a given temperature and composition. The geometry is updated after metal deposition and moving heat source for each time step according to the assumed welding speed. Thus, the numerical mesh used in the simulation had 62 x 132 x 30 in the X (width), Y(length), and Z (depth) directions of plate respectively, however, in the weld region it was used the adaptative meshes technique and refinement to ensure the accuracy of the dynamically weld bead geometric formation corresponding to the dynamic numerical simulation. For the boundary conditions, the effects of convective and radiative fluxes are considered.

The cooling boundary conditions between the workpiece and environment by means of convection and radiation are calculated by Equations (2) and (3), respectively [17-20].

$$q_c = h(T - T_0) \quad (2)$$

$$q_r = \varepsilon(T) \sigma (T^4 - T_0^4) \quad (3)$$

where T_0 ($25^{\circ}C$) is the room temperature, $\varepsilon(T)$ is the emissivity as a function of temperature, σ ($5.67 \times 10^{-8} W.m^{-2}.K^{-4}$) is the Stefan-Boltzmann constant, and h ($15 W.m^{-2}.K^{-1}$) is the natural convective heat coefficient assumed in this study. Paloposki and Liedquist [21] investigated the temperature dependency of emissivity for low carbon steels, but the available data limited for a narrow range of temperature (up to 700 °C). Recent data published by Deus et al. [22] have indicated that a sigmoid function is suitable for applying under welding environment conditions. Thus, the available data by Paloposki and Liedquist [21] can be fitted as shown in Equation 4.

$$\varepsilon(T) = \text{MAX}\left(0.2, \text{MIN}\left(0.65, (0.0016T - 0.7468)\right)\right) \quad (4)$$

The heat input supplied by the torch is modeled by the power distribution given by the well-known moving double-ellipsoid heat source model presented by Goldak et al. (Figure 1) [23]. The model combines two ellipses: one in the front quadrant of the heat source and the other in the rear quadrant. Equations 5 and 6 show the volumetric heat flux distributions inside the front and rear quadrant of the heat source, respectively. The model is defined as a function of position and time together with the parameters that affect the heat flux magnitude and distribution [23].

$$q_r(x, y, z, t) = \frac{6\sqrt{3}f_r Q}{ab_r c \pi \sqrt{\pi}} e^{-3\left(\frac{x(t)}{a}\right)^2} e^{-3\left(\frac{y(t)}{b_r}\right)^2} e^{-3\left(\frac{z(t)}{c}\right)^2} \quad (5)$$

$$q_f(x, y, z, t) = \frac{6\sqrt{3}f_f Q}{ab_f c \pi \sqrt{\pi}} e^{-3\left(\frac{x(t)}{a}\right)^2} e^{-3\left(\frac{y(t)}{b_f}\right)^2} e^{-3\left(\frac{z(t)}{c}\right)^2} \quad (6)$$

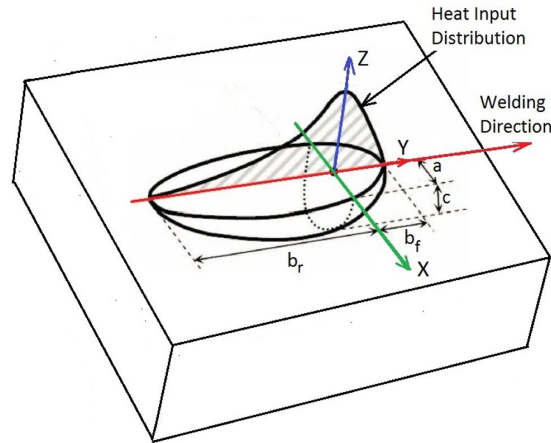


Figure 1. Schematic model for double-ellipsoid heat source [23].

The heat input rate $Q = \eta VI$ is determined by welding operational parameters current (I), voltage (V), and thermal efficiency (η), respectively. The factors f_f and f_r denote the fraction of the heat deposited in the front and rear quadrant, respectively, set up to attain the restriction $f_f + f_r = 2$. The a, b_f, b_r constant source parameters define the size and shape of the ellipses and, therefore, the heat source distribution.

A temperature and composition dependency of the thermophysical properties of the individual phases are assumed in this study. The material properties obey a mixture rule pondered by the local volume fraction of each phase. Equations (7) and (8) are used to dynamically evaluate the heat capacity and the thermal conductivity of the HSLA AISI 4130 steel used in this study during the phase transformations evolution, which considers the mixture rule based on individual phase properties and volume fractions (φ_i).

$$Cp_{(T,\varphi)} = \sum_i \varphi_i Cp_i(T) \quad (7)$$

$$k_{(T,\varphi)} = \sum_i \varphi_i k_i(T) \quad (8)$$

3.2. Solid-state phase transformations

Numerical simulation using a phenomenological kinetic model based on the austenite diffusional transformation during cooling after austenitization of low alloy hypoeutectoid steels was applied to predict the transformations from austenite into ferrite, pearlite, and bainite simultaneously. This section will present some features of the model, and a more detailed description concerning its formulation can be found elsewhere [24]. Thus, the base of the extended version of the multiphase diffusional transformation model of the Avrami-type is represented by Equation 9 [24].

$$\frac{dy_i}{dt} = m_i B_i^{1/m_i} [Y_i - y_i] \left\{ \ln \frac{Y_i}{Y_i - y_i} \right\}^{1-(1/m_i)} \quad (9)$$

The temperature-dependent parameters B_i and m_i are estimated from the TTT diagram for the investigated steel (Figure 2) [25] from the Equations 10 and 11 [24].

$$m_i(T) = \frac{6.1273}{\ln\left(\frac{t_f}{t_s}\right)} \quad (10)$$

$$B_i(T) = \frac{0.01005}{t_s^{m_i(T)}} \quad (11)$$

where t_s and t_f are the times correspondent to 1 and 99% of transformation, respectively.

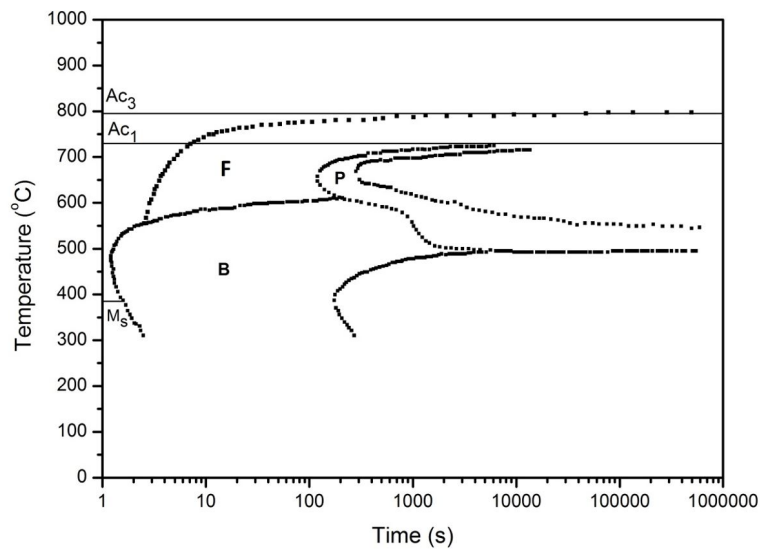


Figure 2. TTT diagram for the HSLA AISI 4130 steel (adapted from Atlas of Time-Temperature Diagrams [25]).

Due to its importance during the austenite diffusional decomposition process, the austenitic grain growth was predicted by the temperature-dependent kinetic equation (Equation 12) [24].

$$\frac{dD}{dt} = \frac{K_A(T)}{n_A D^{n_A-1}} \quad (12)$$

where,

$$K_A(T) = k_A \exp\left[-\frac{E_A}{R(T+273)}\right] \quad (13)$$

In order to include the effect of austenitic grain size in the model, the B_i parameter in Equation 9 is defined by Equation 14 [24].

$$B_i = B_i(T, D) = B_i(T) \left(\frac{D_{ref}}{D}\right)^{\varepsilon_i} \quad (14)$$

Based on the works of Reti et al. [24] and Gergely et al. [26], in Equations 12 to 14 n_A was assumed as 2.44; k_A as 6.087×10^7 , ε_i are positive constants varying between 0.6 and 1.3 and depends upon the transformation type, i.e., ferrite, pearlite or bainite and E_A which correspond the activation energy for the growth process, the value of 317 kJ.mol^{-1} . R is the universal gas constant ($8.314 \text{ J.K}^{-1}.\text{mol}^{-1}$); $B_i(T)$ parameter is obtained from the TTT diagram of the investigated steel by means of Equation 11 and D_{ref} corresponds to the reference grain diameter (0.0159 mm).

After some modifications in order to take into account the coupling effects among the individual phase transformation process, the multiphase model has its final form represented by the coupled system of the differential Equations 15 to 19 [24].

$$\frac{dy_1}{dt} = m_1 K_1^{1/m_1} [Y_{Fe} - y_1] \left(\ln \frac{Y_{Fe}}{Y_{Fe} - y_1} \right)^{1-(1/m_1)} H(Y_{Fe} - y_1) \quad (15)$$

$$\frac{dy_2}{dt} = m_2 K_2^{1/m_2} [Y_{Pe} - y_2] \left(\ln \frac{Y_{Pe}}{Y_{Pe} - y_2} \right)^{1-(1/m_2)} H(Y_{Pe} - y_2) \quad (16)$$

$$\frac{dy_3}{dt} = m_3 K_3^{1/m_3} [Y_{Ba} - y_1 - y_3] \left(\ln \frac{Y_{Ba}}{Y_{Ba} - y_1 - y_3} \right)^{1-(1/m_3)} H(Y_{Ba} - y_3) \quad (17)$$

$$\frac{dy_4}{dt} = m_4 K_4^{1/m_4} [Y_{Ba} - y_1 - y_2 - y_3 - y_4] \left(\ln \frac{Y_{Ba} - y_1 - y_2 - y_3}{Y_{Ba} - y_2 - y_3 - y_4} \right)^{1-(1/m_4)} H(Y_{Ba} - y_4) \quad (18)$$

$$\frac{dD}{dt} = \frac{K_A(T)}{n_A D^{n_A - 1}} \quad (19)$$

where y_1 , y_2 , y_3 and y_4 correspond to the products from austenite transformation, namely, ferrite, pearlite, upper and lower bainite, respectively; $H(x)$ is the Heaviside function (in order to take into account the irreversibility of the process); m_1 , m_2 , m_3 and m_4 are parameters temperature-dependent obtained from the isothermal diagram of the investigated steel using Equation 10; Y_{Fe} , Y_{Pe} and Y_{Ba} correspond to maximum volume fractions of ferrite, pearlite, and bainite respectively (Figure 3), calculated in accord to the methodology proposed by Babu and Prasanna Kumar [27], whereas K_1 , K_2 , K_3 and K_4 are functions defined by Equation 20 [24].

$$K_i = K_i(T, D) = B_i(T) \left(\frac{D_{ref}}{D} \right)^{\epsilon_i} \quad (20)$$

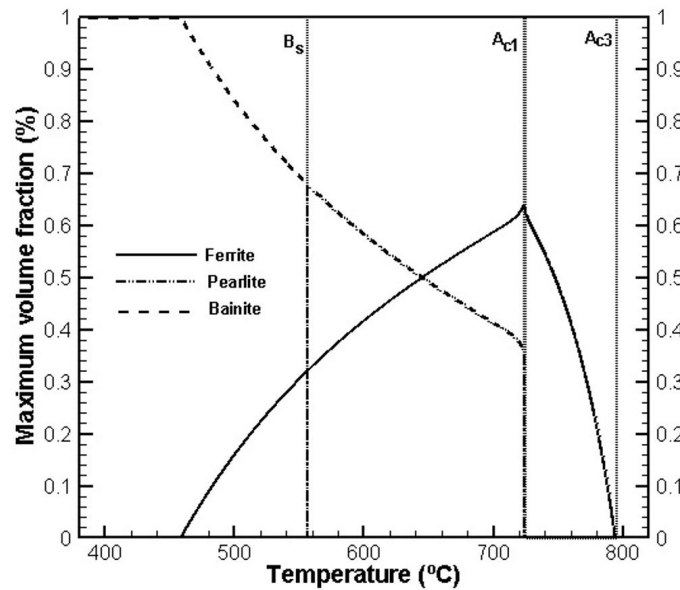


Figure 3. Maximum volume fractions of ferrite, pearlite, and bainite for the HSLA AISI 4130 steel.

Meanwhile, the volume fraction of martensite was calculated using a novel model (Equation 21) proposed by Lee and van Tyne [28], which has been based on the optimization of well-known Koistinen-Marburger model by the introduction of two parameters, K_{LV} and n_{LV} , therefore, allowing to take into account the steel composition effects on the kinetic.

$$V_m = 1 - \exp \left[-K_{LV} (M_s - T)^{n_{LV}} \right] \quad (21)$$

where V_m is the volume fraction of martensite; T is the absolute temperature; M_s is the martensite start temperature and,

$$K_{LV}(K^{-1}) = 0.0231 - 0.0105C - 0.0017Ni + 0.0074Cr - 0.0193Mo \quad (22)$$

$$n_{LV} = 1.4304 - 1.1836C + 0.7527C^2 - 0.0258Ni - 0.0739Cr + 0.3108Mo \quad (23)$$

3.3. Solidification microstructure parameters

The primary and secondary dendrite arm spacing (PDAS) and (SDAS) respectively at the fusion zone are modeled based on the Equations 24 and 25, respectively.

$$\lambda_1 = K_1(G_L v_L)^{-0.5} \quad (24)$$

$$\lambda_2 = K_2(G_L v_L)^{-0.34} \quad (25)$$

The model parameters are experimentally determined, where K_1 and K_2 are functions of solute concentrations, G_L the temperature local gradient at the supercooled liquid, and v_L the speed of the solid-liquid front dynamically evaluated in the representative volume during the transformation. The parameters K_1 (15.2) and K_2 (6.2) were determined using inverse numerical method by optimization of the spatial dendrites spacing prediction errors using the measured values obtained during microstructural analysis of the bead regions.

3.4. Hardness distribution

The hardness distribution at the HAZ of investigated steel was calculated using the rule of mixtures (Equation 26).

$$H_v = X_M H_{vM} + X_B H_{vB} + (X_F + X_P) H_{vF+P} \quad (26)$$

where H_v is the hardness (Vickers); X_M , X_B , X_F and X_P are the volume fractions of martensite, bainite, ferrite, and pearlite, respectively; H_{vM} , H_{vB} and H_{vF+P} are the hardness of martensite, bainite, and the mixture of ferrite and pearlite, respectively.

For the calculating of H_{vM} , H_{vB} and H_{vF+P} were used the formulae developed by Maynier et al. [29] (Equations 27 to 29), which take into account the steel composition and the cooling rate.

$$H_{vM} = 127 + 949C + 27Si + 11Mn + 8Ni + 16Cr + 21 \log Vr \quad (27)$$

$$H_{vB} = -323 + 185C + 330Si + 153Mn + 65Ni + 144Cr + 191Mo + (89 + 53C - 55Si - 22Mn - 10Ni - 20Cr - 33Mo) \log Vr \quad (28)$$

$$H_{vF+P} = 42 + 223C + 53Si + 30Mn + 12.6Ni + 7Cr + 19Mo + (10 - 19Si + 4Ni + 8Cr + 130V) \log Vr \quad (29)$$

$$Vr = \left(\frac{\partial T}{\partial t} \right)_{700} \approx \left(\frac{T_t - T_t - \Delta t}{\Delta t} \right)_{700} \quad (30)$$

where Vr is the cooling rate at 700°C in $^{\circ}C.h^{-1}$ and Δt is the numerical time step assumed during the calculations.

4. Results and Discussion

4.1. Thermal features

From the comparison between the calculated and measured dimensions of the FZ and HAZ in Figure 4a-c, it is possible to conclude the accuracy of the used model, as well as the precise definition and application of the boundary conditions of the heat source parameters and on the material metallurgical and thermophysical features used in this study. Thus, it allows the applicability of the model for temperature and welding zone predictions and, accordingly, providing reliable data for the calculations of phase volume fractions, solidification microstructure, and hardness in HSLA steel welds.

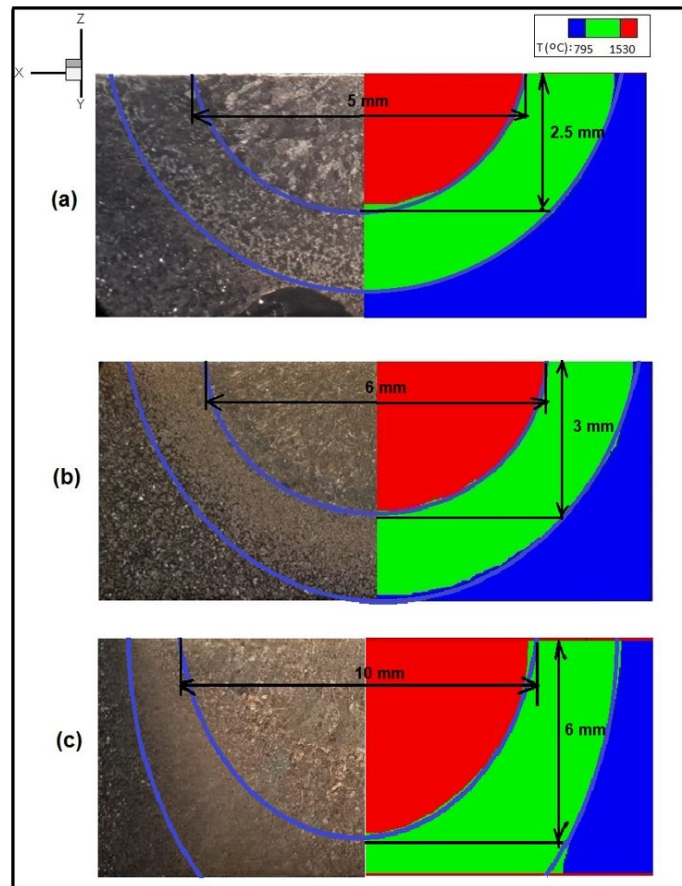


Figure 4. Calculated and measured dimensions of the FZ and HAZ: (a) 0.5 kJ mm^{-1} ; (b) 0.5 kJ mm^{-1} (with preheating), and (c) 2.0 kJ mm^{-1} .

Figure 5a-c shows the results for three-dimensional transient temperature distributions when the welding heat source already traveled an identical distance along the workpieces in each welding condition considered in this study (see Table 2). In lower heat input, the temperature distribution is more concentrated around the weld regions HAZ and FZ and higher thermal gradients will occur in the workpiece. These phenomena will directly influence the cooling rates and, accordingly, on the phase transformations and the weldment properties, as the hardness distribution at the HAZ will be presented in the next sections.

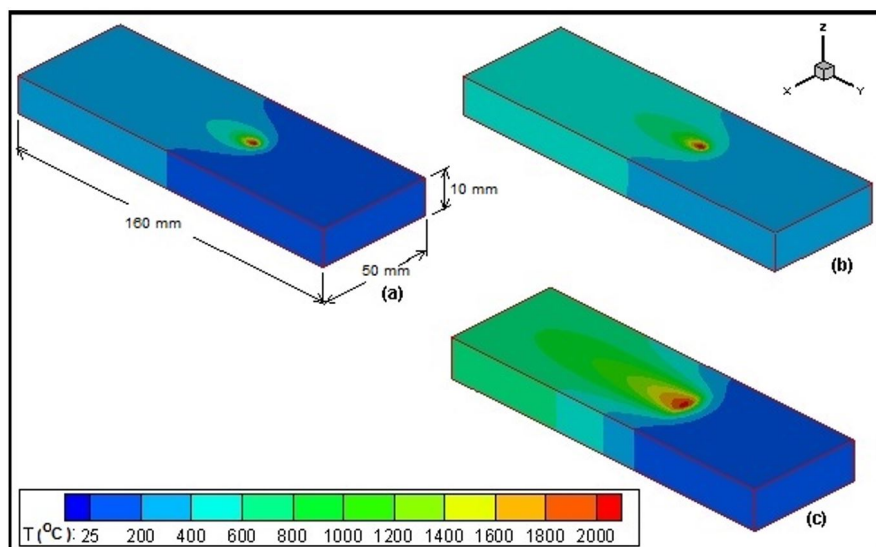


Figure 5. Calculated 3-D temperature distribution during welding: (a) 0.5 kJ mm^{-1} ; (b) 0.5 kJ mm^{-1} (with preheating) and (c) 2.0 kJ mm^{-1} .

Figures 6a-c show the profile and the intensity of the cooling rates acting along with the workpieces in a plane corresponding to its centerline in the welding direction. The preheating effect has resulted in lower cooling rates when comparing identical heat inputs (Figures 6a and b), and the same behavior will also be observed when comparing different levels of heat input (Figures 6a and c). These results are direct consequences of lower thermal gradients that are produced in both comparative situations. Since that the heat input magnitude and workpiece preheating effects act on its heating and cooling rates, material metallurgical parameters as grain size will be affected, and these, in your turn, will play a decisive role in the phase transformations. These combinations of causes and effects will be decisive on the kind and characteristics of obtained microstructure in the weld regions, as at the HAZ and FZ and, accordingly, on the weldment properties, as will be presented in the next sections.

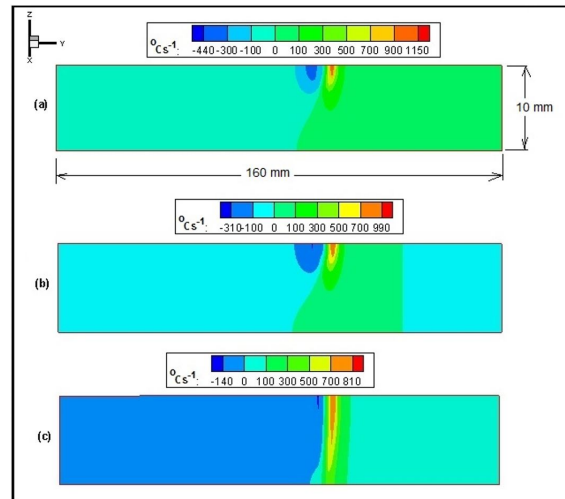


Figure 6. Calculated local cooling and heating rates: (a) 0.5 kJ mm⁻¹; (b) 0.5 kJ mm⁻¹(with preheating) and (c) 2.0 kJ mm⁻¹.

4.2. Solid-state phase transformations and grain growth

Figures 7a-c to 10a-c present the microstructures calculated at the HAZ in all the evaluated conditions in this study. The results are in good agreement with the experimental one, including the hardness, as will be seen in the next sections. Figures 7a to 10a correspond to the lowest heat input evaluated and, accordingly, are the case where the greatest cooling rates are obtained, justifying the highest martensite fraction. Although in Figures 7b to 10b the heat input used had been the same as in Figures 7a to 10a, the use of preheating led to the lower cooling rates, exactly as has occurred in Figures 7c to 10c, whose used heat input was the highest among all, justifying the lower observed martensite fractions in Figures 7b-c to 10b-c respectively. Thus, the martensite fraction will decrease (Figures 7b-c to 10b-c), while the fractions of other constituents, such as bainite and ferrite, will be increased obviously. It is worth mentioning that it was not possible to separately evaluate the fractions of upper and lower bainite due to the difficulty of individual isolating of these constituents in the microstructure. Meanwhile, the fractions of constituents at the HAZ were 90% (Standard Deviation (SD) of 10%) for martensite and 5% (SD of 2%) for bainite in samples with 0.5 kJ mm⁻¹; 45% (SD of 5%) for martensite, 50% (SD of 5%) for bainite and 20% (SD of 3%) for ferrite in samples with 0.5 kJ mm⁻¹ (with preheating) and 10% (SD of 2%) for martensite, 70% (SD of 8%) for bainite and 20% (SD of 4%) for ferrite in samples with 2.0 kJ mm⁻¹. Representative microstructures of these observations using LOM and SEM can be seen in Figures 11a-b to 13a-b, respectively.

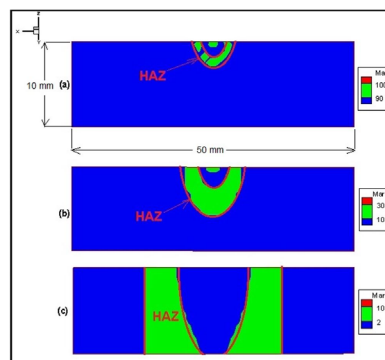


Figure 7. Calculated martensite at the HAZ: (a) 0.5 kJ mm⁻¹; (b) 0.5 kJ mm⁻¹ (with preheating) and (c) 2.0 kJ mm⁻¹.

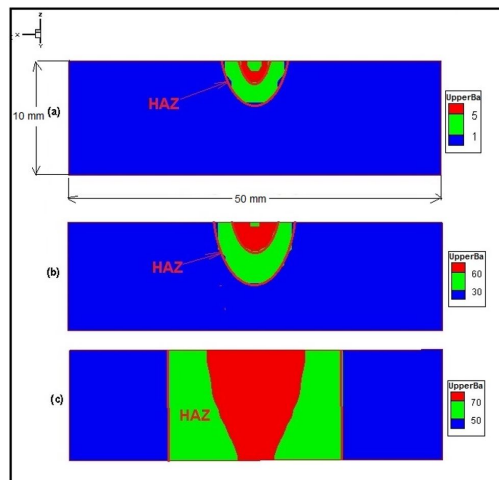


Figure 8. Calculated upper bainite at the HAZ: (a) 0.5 kJ mm⁻¹; (b) 0.5 kJ mm⁻¹ (with preheating) and (c) 2.0 kJ mm⁻¹.

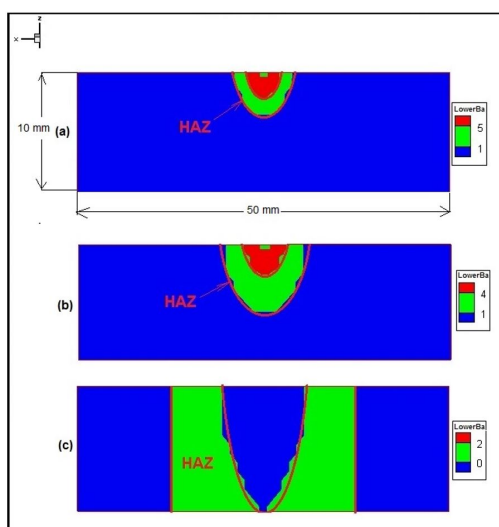


Figure 9. Calculated lower bainite at the HAZ: (a) 0.5 kJ mm⁻¹; (b) 0.5 kJ mm⁻¹ (with preheating) and (c) 2.0 kJ mm⁻¹.

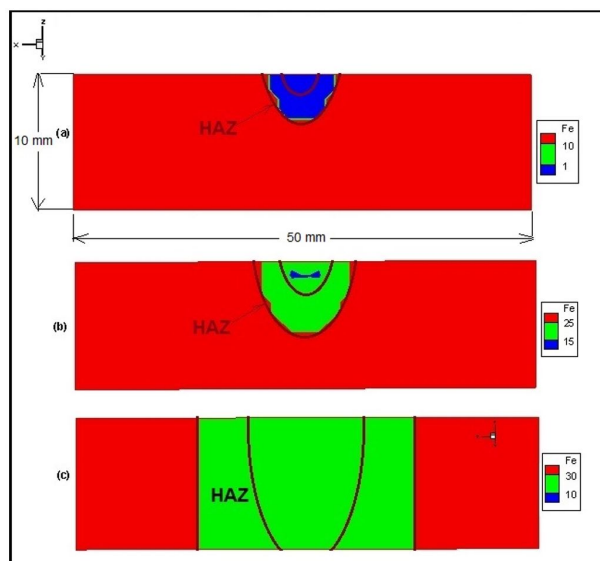


Figure 10. Calculated ferrite at the HAZ: (a) 0.5 kJ mm⁻¹; (b) 0.5 kJ mm⁻¹ (with preheating) and (c) 2.0 kJ mm⁻¹.

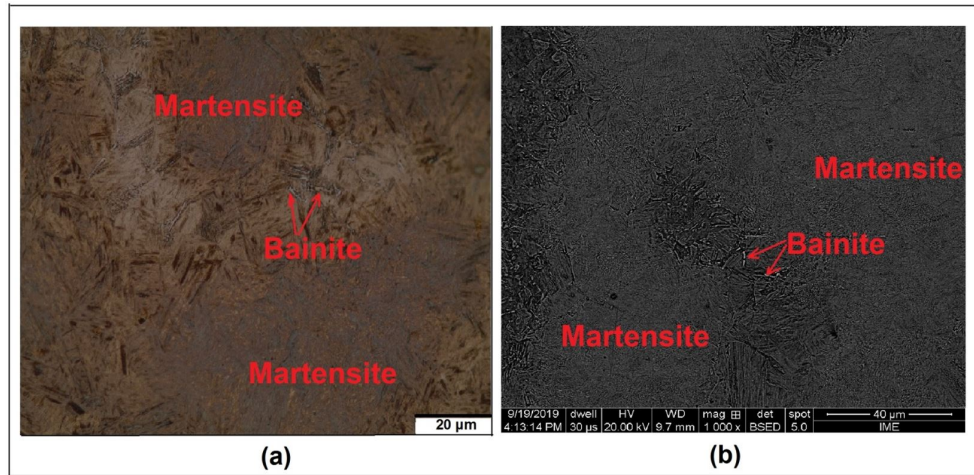


Figure 11. Representative (a) LOM and (b) SEM of the HAZ of 0.5 kJ mm⁻¹ sample.

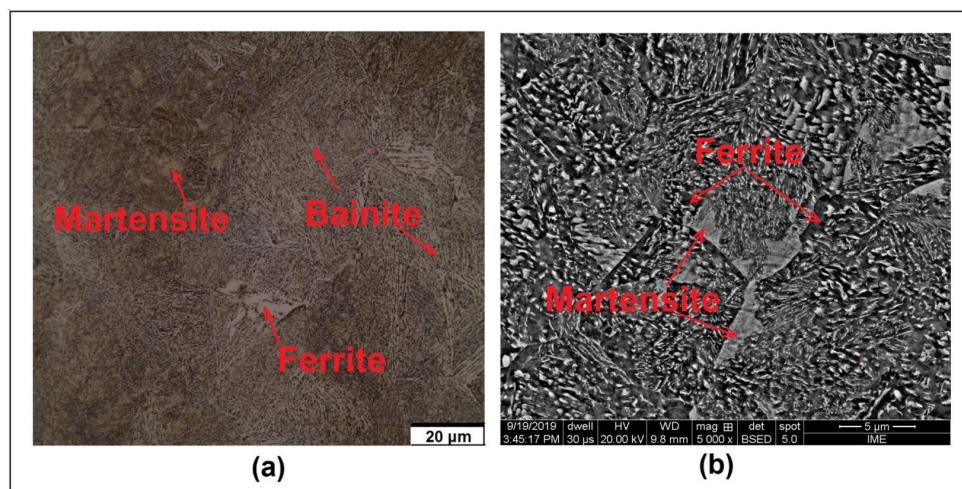


Figure 12. Representative (a) LOM and (b) SEM of the HAZ of 0.5 kJ mm⁻¹ (with preheating) sample.

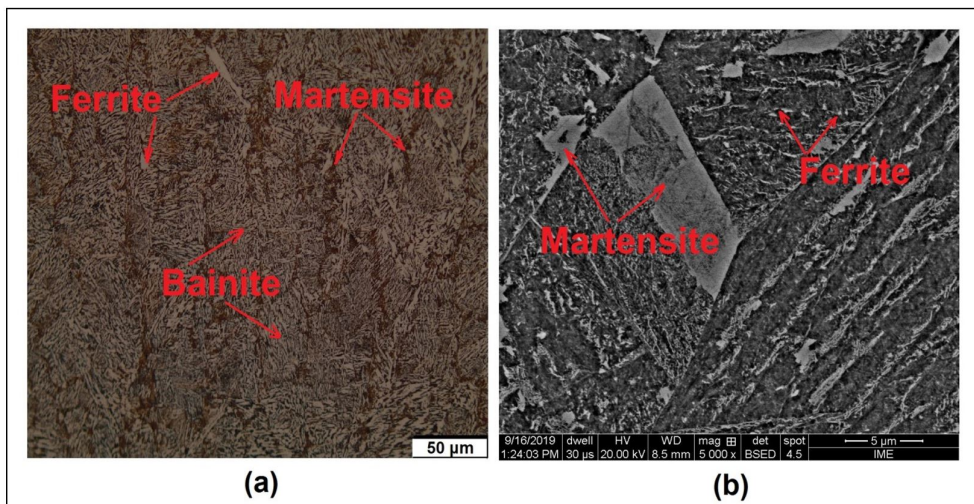


Figure 13. Representative (a) LOM and (b) SEM of the HAZ of 2.0 kJ mm⁻¹ sample.

The base metal grain size was 20 μm, but it has undergone changes due to the welding procedure. Calculated grain sizes at the HAZ for all conditions evaluated in this study are shown in Figure 14. Due to the microstructural interference, it was very difficult to outline the grain boundary in the sample of 0.5 kJ mm⁻¹ (with and without preheating). Therefore, it was only possible to measure the grain size in the experiment using 2 kJ mm⁻¹. The chosen local to carry out the measuring was the High-

Temperature Heat Affected Zone (HTHAZ), i.e., near the FZ, and the found result was $67 \mu\text{m}$ (SD of $3 \mu\text{m}$). Therefore, presenting a good agreement with the calculated result in Figure 14a. Cooling and heating rates are intrinsically associated with the heat input magnitude and its effects directly affect the final grain size in weldment regions such as the HAZ. Due to the comparatively longer time exposed to elevated temperatures, the final grain size was larger when lower cooling rates were reached (see Figure 6a-c), i.e., when using the heat input of 2.0 kJ mm^{-1} . Likewise, preheating has also promoted a slight increase in the grain size when compared with the same heat input (0.5 kJ mm^{-1}). Figure 15 is a representative micrograph from the HTHAZ in 2.0 kJ mm^{-1} sample, where the grain boundaries (GB) in this weld region can be clearly seen.

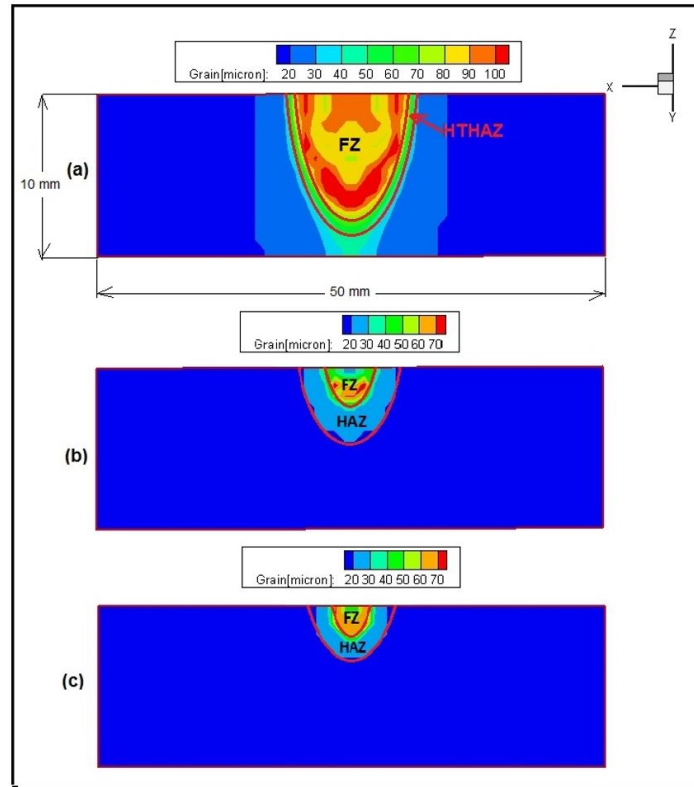


Figure 14. Calculated grain size: (a) 2.0 kJ mm^{-1} ; (b) 0.5 kJ mm^{-1} (with preheating) and (c) 0.5 kJ mm^{-1} .

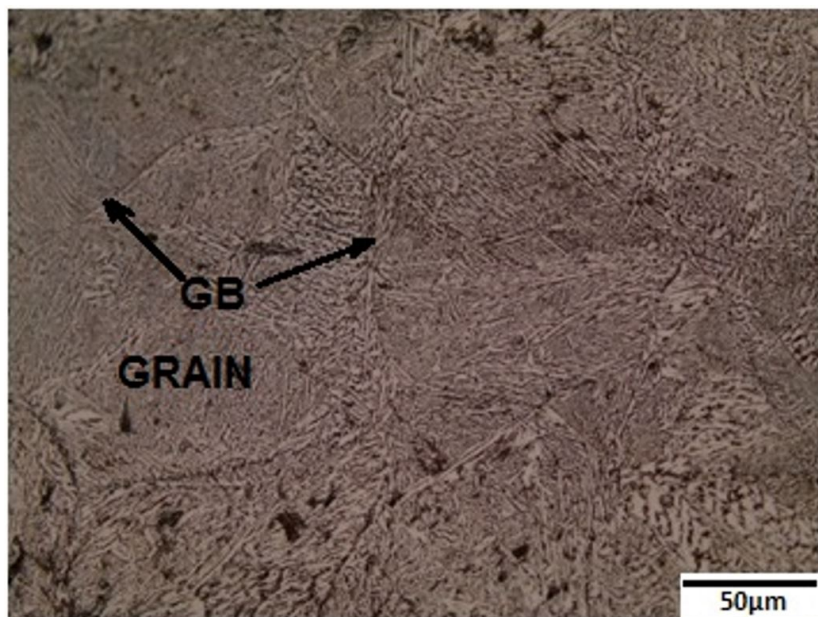


Figure 15. Grain boundaries by LOM in HTHAZ of 2.0 kJ mm^{-1} sample

4.3. Solidification microstructure

Experimental dendrite arms spacing measures at the FZ are shown in Table 3, except for the secondary spacing from the 0.5 kJ mm⁻¹ samples (with and without preheating), since it was too difficult to get a satisfactory resolution to carry out the metallographic analysis due to the interference from constituents present in the microstructure. Meanwhile, it was possible to calculate both secondary and primary dendrite arms spacing for all welding conditions evaluated in this study and the corresponding results can be seen in Figures 16 to 18. Furthermore, the calculated results have shown a good agreement with the experimental one. How it can be seen in Table 3 and Figures 16 to 18, greater spacings among dendrites arms were obtained with higher heat input or when using preheating, i.e., welding procedures that favor the occurrence of lower thermal gradients in the workpiece.

Table 3. Experimental measures from dendrite arm spacing.

Sample (kJ mm ⁻¹)	Primary arm (mean value) (μm)	Secondary arm (mean value) (μm)
0.5	7 (SD* = 0.33)	-
0.5 (with preheating)	12 (SD* = 0.57)	-
2.0	35 (SD* = 0.6)	19 (SD* = 0.76)

*Standard Deviation.

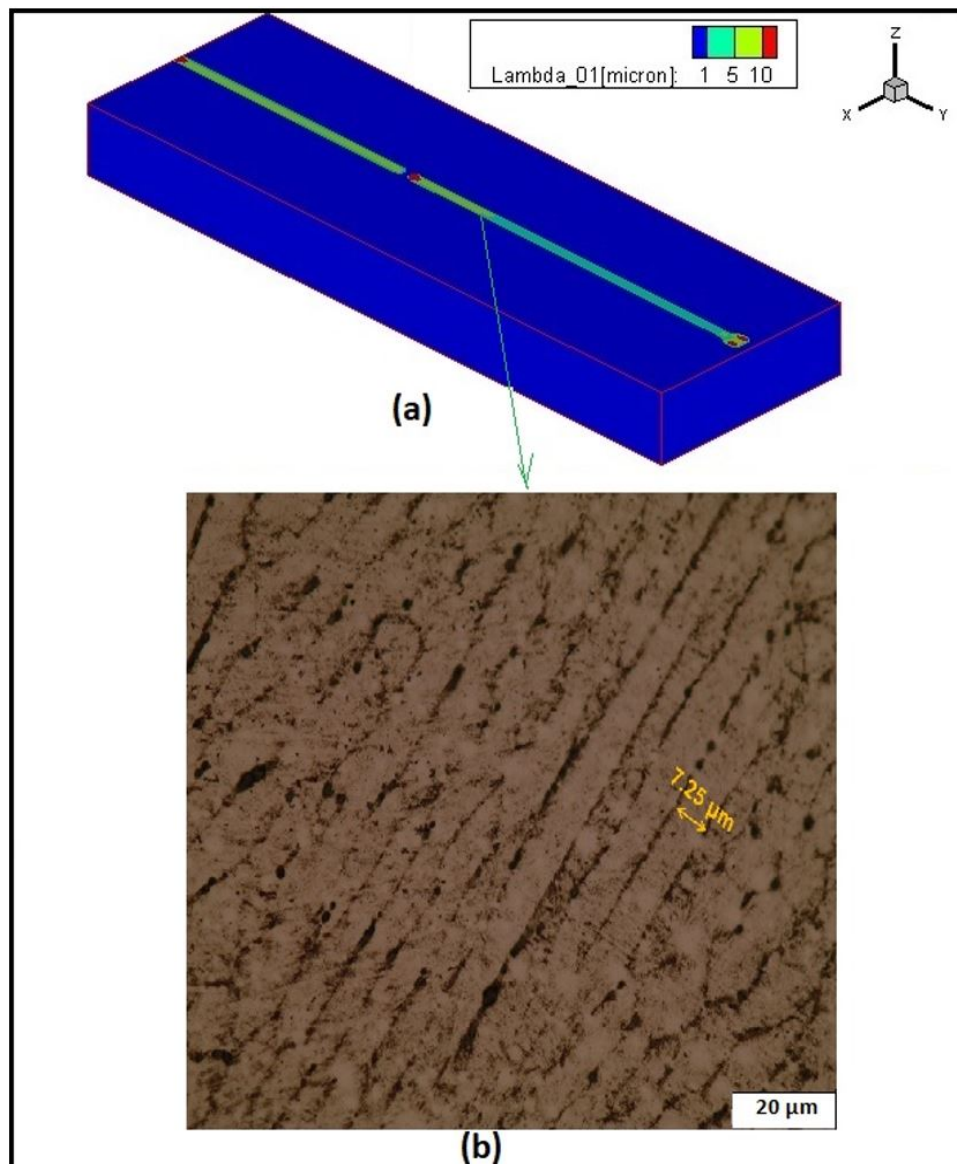


Figure 16. (a) Calculated and (b) experimental dendrite primary arm spacing (0.5 kJ mm⁻¹).

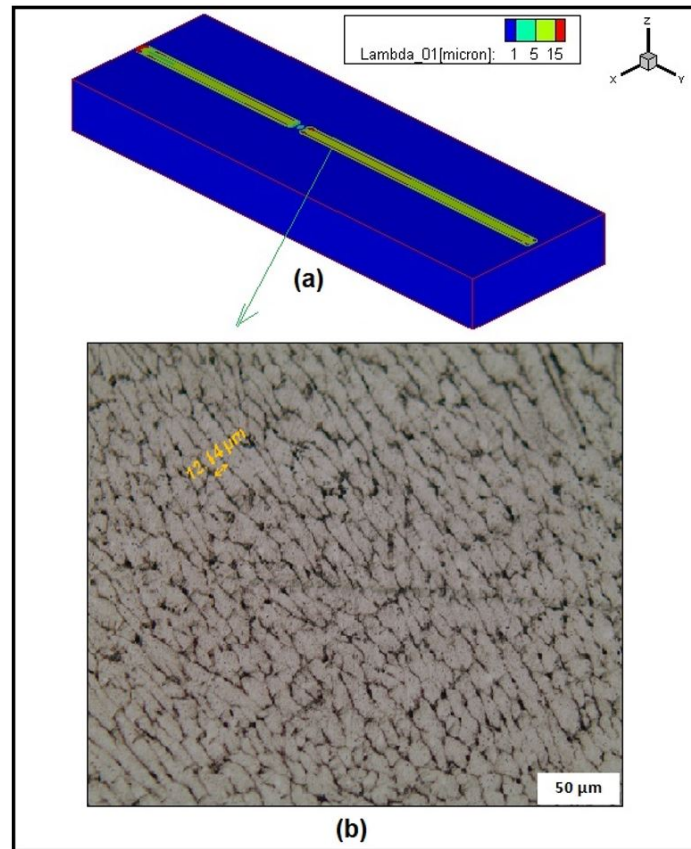


Figure 17. (a) Calculated and (b) experimental dendrite primary arm spacing (0.5 kJ mm^{-1} with preheating).

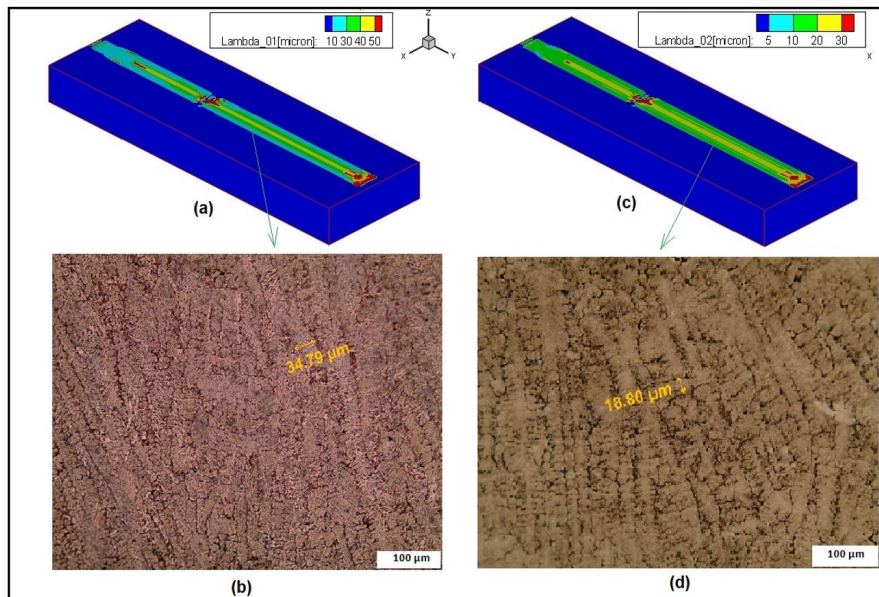


Figure 18. (a) Calculated and (b) experimental dendrite primary arm spacing. (c) Calculated and (d) experimental dendrite secondary arm spacing. (2.0 kJ mm^{-1}).

4.4. Hardness

A comparison between the measured and calculated hardness in a transverse section of the plates can be seen in Figures 19 to 21. It is important to note that the interest region in this analysis is the HAZ with the measurements and calculations performed at the plate surface where welding was carried out. Greater hardness levels have been achieved at the HAZ when using lower heat input since it favors the obtaining of greater cooling rates which, in your turn, will favor the harder constituents formation, as the martensite. On the other hand, Figure 20 shows the effects of preheating on the HAZ hardness in comparison with the results

presented in Figure 19, when in both situations it was used the same heat input (0.5 kJ mm^{-1}). Preheating has favored lower thermal gradients in the workpiece to occur and, accordingly, lower cooling rates, comparatively resulting in fractions minor of harder constituents, as the martensite (see Figures 7 to 10). Finally, a good agreement was obtained between the calculated and experimental results, enabling the used model to calculate the hardness distribution at the HAZ in HSLA steel welds.

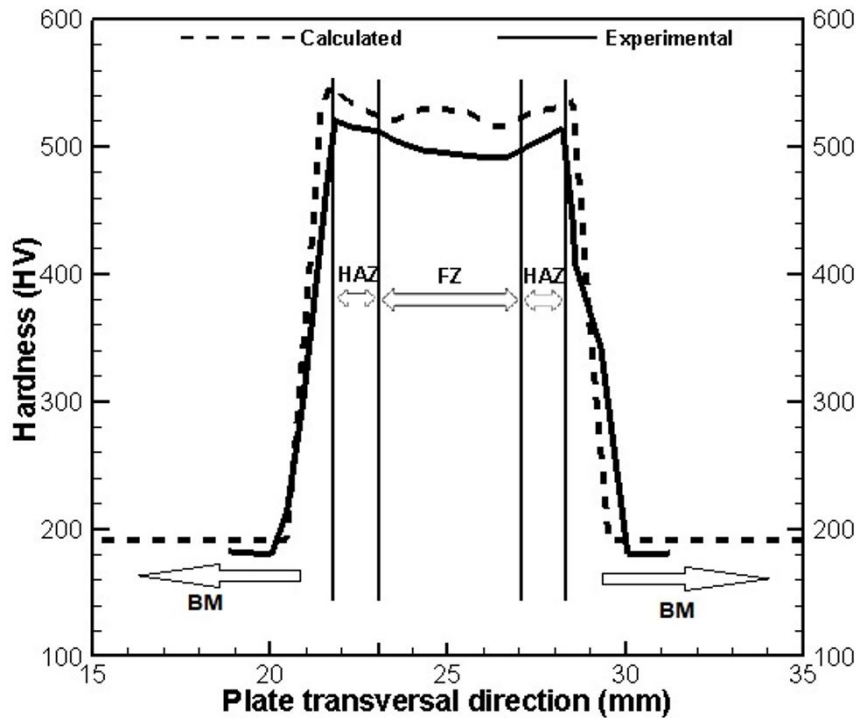


Figure 19. Calculated and experimental hardness (0.5 kJ mm^{-1}).

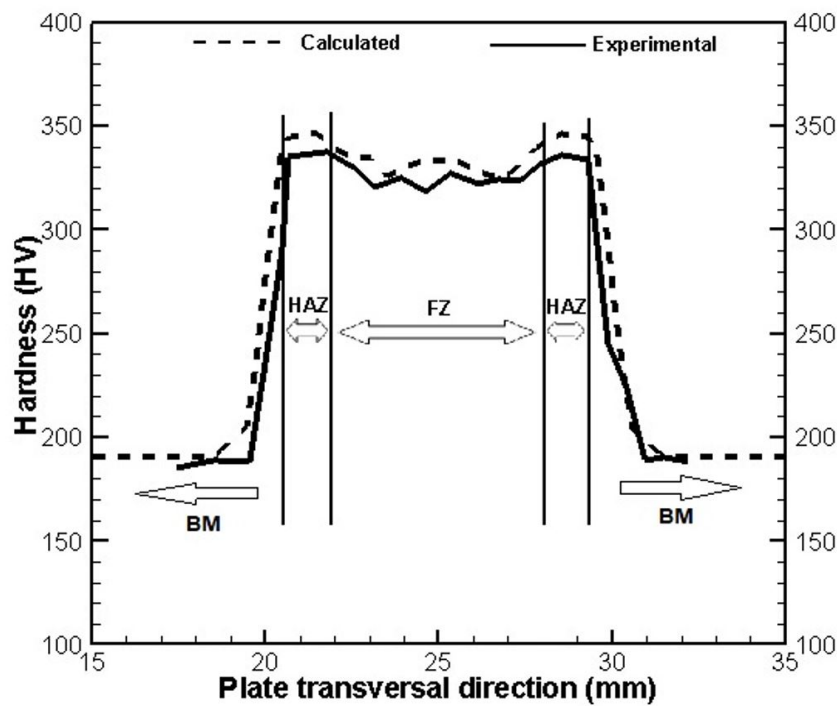


Figure 20. Calculated and experimental hardness (0.5 kJ mm^{-1} with preheating).

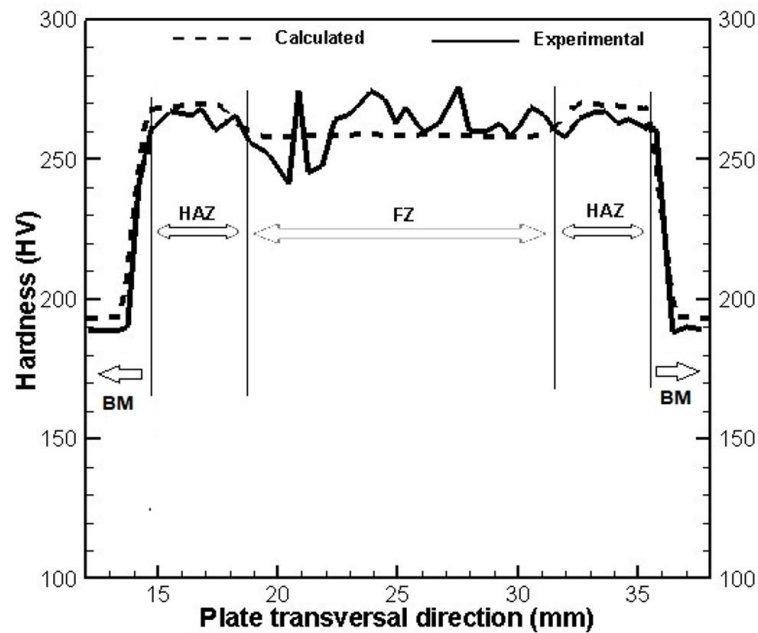


Figure 21. Calculated and experimental hardness (2.0 kJ mm^{-1}).

5. Conclusions

A coupled thermo-mechanical-metallurgical model was implemented in an in-house computational code based on the FVM and applied to numerically simulate the thermal history, the solid-state phase transformations, the solidification microstructure and the hardness in welds performed on a HSLA AISI 4130 steel. Thus, the results are summarized as follows.

- a) The model demonstrated great accuracy in reproducing the thermal history from the welding;
- b) The numerical methodology was able to closely predict the FZ and HAZ shapes and dimensions;
- c) The numerical methodology was able to closely predicting the solid-state phase transformations and quantify the constituents at the resulting microstructure;
- d) The numerical methodology was able to predict the grain growth at the HAZ closely;
- e) The numerical methodology was able to closely predicting and calculating the formation and the dendrite arm spacing at the FZ;
- f) The numerical methodology was able to predict the hardness distribution at the HAZ closely.

Acknowledgements

This work was partially supported by CNPq, FAPERJ and CAPES.

References

- [1] Zinigrad M, Borodianskiy K. Welding, joining, and coating of metallic materials. *Materials (Basel)*. 2020;13(11):2640. <http://dx.doi.org/10.3390/ma13112640>. PMID:32531875.
- [2] Grong Ø, Shercliff HR. Microstructural modelling in metals processing. *Progress in Materials Science*. 2002;47(2):163-282. [http://dx.doi.org/10.1016/S0079-6425\(00\)00004-9](http://dx.doi.org/10.1016/S0079-6425(00)00004-9).
- [3] Zacharia T, Vitek JM, Goldak JA, DebRoy TA, Rappaz M, Bhadeshia HKDH. Modeling of fundamental phenomena in welds. *Modelling and Simulation in Materials Science and Engineering*. 1995;3(2):265-288. <http://dx.doi.org/10.1088/0965-0393/3/2/009>.
- [4] Ahmad B, Galloway A, Toumpis A. Advanced numerical modelling of friction stir welded low alloy steel. *Journal of Manufacturing Processes*. 2018;34:625-636. <http://dx.doi.org/10.1016/j.jmapro.2018.07.003>.
- [5] Jedrasiak P, Shercliff HR, McAndrew AR, Colegrove PA. Thermal modelling of linear friction welding. *Materials & Design*. 2018;156:362-369. <http://dx.doi.org/10.1016/j.matdes.2018.06.043>.
- [6] Yu F, Wei Y, Ji Y, Chen LQ. Phase field modeling of solidification microstructure evolution during welding. *Journal of Materials Processing Technology*. 2018;255:285-293. <http://dx.doi.org/10.1016/j.jmatprotec.2017.12.007>.
- [7] Zhang B, Chen X, Pan KX, Li M, Wang JN. Thermo-mechanical simulation using microstructure-based modeling of friction stir spot welded AA 6061-T6. *Journal of Manufacturing Processes*. 2019;37:71-81. <http://dx.doi.org/10.1016/j.jmapro.2018.11.010>.

- [8] Eyvazian A, Hamouda A, Tarlochan F, Derazkola HA, Khodabakhshi F. Simulation and experimental study of underwater dissimilar friction-stir welding between aluminium and steel. *Journal of Materials Research and Technology*. 2020;9(3):3767-3781. <http://dx.doi.org/10.1016/j.jmrt.2020.02.003>.
- [9] Costa PS, Reyes-Valdés FA, Saldaña-Garcés R, González-González DS, Delgado-Albavera ER. Optimización de los Parámetros de Soldadura por Arco Sumergido en Acero HSLA: una Aplicación para Manufactura de Tuberías de Conducción de Hidrocarburos. *Soldagem e Inspeção*. 2015;20(4):456-466. <http://dx.doi.org/10.1590/0104-9224/SI2004.12>.
- [10] Neto FS, Neves D, Silva OMM, Lima MSF, Abdalla AJ. An analysis of the mechanical behavior of AISI 4130 steel after tig and laser welding process. *Procedia Engineering*. 2015;114:181-188. <http://dx.doi.org/10.1016/j.proeng.2015.08.057>.
- [11] Tseng KH, Shiu YJ. Effect of thermal stability of powdered oxide on joint penetration and metallurgical feature of AISI 4130 steel TIG weldment. *Powder Technology*. 2015;286:31-38. <http://dx.doi.org/10.1016/j.powtec.2015.07.047>.
- [12] Emamian A, Emamian A, Kowkabi AH. Effects of fillerwire composition along with different pre- and post-heat treatment on mechanical properties of AISI 4130 welded by the GTAW process. *Materials Sciences and Applications*. 2010;1(3):135-140. <http://dx.doi.org/10.4236/msa.2010.13022>.
- [13] Nascimento MP, Voorwald HJC, Payão JC Fo. Fatigue strength of tungsten inert gas-repaired weld joints in airplane critical structures. *Journal of Materials Processing Technology*. 2011;211(6):1126-1135. <http://dx.doi.org/10.1016/j.jmatprotec.2011.01.016>.
- [14] Saadati M, Edalat Nobarzad AK, Jahazi M. On the hot cracking of HSLA steel welds: role of epitaxial growth and HAZ grain size. *Journal of Manufacturing Processes*. 2019;41:242-251. <http://dx.doi.org/10.1016/j.jmapro.2019.03.032>.
- [15] Di X, Deng S, Wang B. Effect of pulse current on mechanical properties and dendritic morphology of modified medium manganese steel welds metal. *Materials & Design*. 2015;66:169-175. <http://dx.doi.org/10.1016/j.matdes.2014.10.050>.
- [16] Yang J, Wang Y, Li F, Huang W, Jing G, Wang Z, et al. Weldability, microstructure and mechanical properties of laser-welded selective laser melted 304 stainless steel joints. *Journal of Materials Science and Technology*. 2019;35(9):1817-1824. <http://dx.doi.org/10.1016/j.jmst.2019.04.017>.
- [17] Xavier CR, Delgado HG Jr, Castro JA, Ferreira AF. Numerical predictions for the thermal history, microstructure and hardness distributions at the HAZ during welding of low alloy steels. *Materials Research*. 2016;19(3):520-533. <http://dx.doi.org/10.1590/1980-5373-MR-2015-0068>.
- [18] Xavier CR, Delgado HG Jr, Castro JA. An experimental and numerical approach for the welding effects on the duplex stainless steel microstructure. *Materials Research*. 2015;18(3):489-502. <http://dx.doi.org/10.1590/1516-1439.302014>.
- [19] Xavier CR, Campos MF, Castro JA. Numerical method applied to duplex stainless steel. *Ironmaking & Steelmaking*. 2013;40(6):420-429. <http://dx.doi.org/10.1179/1743281212Y.0000000065>.
- [20] Xavier CR, Junior HGD, Castro JA. Numerical evaluation of the weldability of the low alloy ferritic steels T/P23 and T/P24. *Materials Research*. 2011;14(1):73-90. <http://dx.doi.org/10.1590/S1516-14392011005000019>.
- [21] Paloposki T, Liedquist L. Steel emissivity at high temperatures. *VTT Research Notes*. Finland: VTT Technical Research Centre of Finland; 2005. p. 1-81.
- [22] Deus VS, Castro JA, Correa SR. Correlation among the input thermal parameters and thermography measurements data of the resistance seam welding. *Materials Research*. 2020;23(1):1-7. <http://dx.doi.org/10.1590/1980-5373-mr-2020-0029>.
- [23] Goldak J, Chakravarti A, Bibby M. A new finite element model for welding heat sources. *Metallurgical and Materials Transactions B*. 1984;15:299-305. <http://dx.doi.org/10.1007/BF02667333>.
- [24] Reti T, Fried Z, Felde I. Computer simulation of steel quenching process using a multi-phase transformation model. *Computational Materials Science*. 2001;22(3-4):261-278. [http://dx.doi.org/10.1016/S0927-0256\(01\)00240-3](http://dx.doi.org/10.1016/S0927-0256(01)00240-3).
- [25] ASM International. Atlas of time-temperature diagrams. Vol. 1. Dusseldorf, Germany: Verlag Stahleisen mbH; 1954. p. 139.
- [26] Gergely M, Somogyi S, Réti T, Konkoly T. Computerized properties prediction and technology planning in heat treatment of steels. In: ASM International, ed. *ASM Handbook*. Vol. 4. Materials Park, OH: ASM International; 1991, p. 638-656.
- [27] Babu K, Prasanna Kumar TS Comparison of austenite decomposition models during finite element simulation of water quenching and air cooling of AISI 4140 steels. *Metallurgical and Materials Transactions B*, 2014;45(B):1530-1544. <http://dx.doi.org/10.1007/s11663-014-0069-0>.
- [28] Lee SJ, van Tyne CJ. A kinetics model for martensite transformation in plain carbon and low-alloyed steels. *Metallurgical and Materials Transactions A*. 2012;43:422-427. <http://dx.doi.org/10.1007/s11661-011-0872-z>.
- [29] Maynier P, Dollet J, Bastien P. Hardenability concepts with applications to steels. In: Doane DV, Kirkaldy JS, editors. *The Metallurgical Society of AIME*. New York: AIME; 1978, p. 518-544.